

Article

Tailoring Magnetic Properties and Magnetoimpedance Response in Nanocrystalline $(\text{Fe}_3\text{Ni})_{81}\text{Nb}_7\text{B}_{12}$ Ribbons for Sensor Applications

David González-Alonso ^{1,2,*} , Lorena Gonzalez-Legarreta ^{3,4,5,*} , Jozef Marcin ⁵, Peter Švec ⁶  and Ivan Škorvánek ⁵ 

- ¹ Departamento de Física Aplicada, Facultad de Ciencias, Universidad de Cantabria, Avda. de Los Castros 48, 39005 Santander, Spain
- ² Institute of Physics, Faculty of Science, P.J. Šafárik University, Park Angelinum 9, 04154 Košice, Slovakia
- ³ Departamento de QUIPRE, Universidad de Cantabria, Avda. de Los Castros 46, 39005 Santander, Spain
- ⁴ Nanomedicine Group, IDIVAL, Avda. Cardenal Herrera Oria s/n, 39011 Santander, Spain
- ⁵ Institute of Experimental Physics, Slovak Academy of Sciences, 04001 Košice, Slovakia
- ⁶ Institute of Physics, Slovak Academy of Sciences, 84511 Bratislava, Slovakia
- * Correspondence: david.gonzalezalonso@unican.es (D.G.-A.); gonzalezll@unican.es (L.G.-L.)

Abstract: Today, there is an increasing demand for progress in the magnetoimpedance (MI) response of cost-effective soft-magnetic materials for use in high-performance sensing devices. In view of this, we investigate here the field-annealing effects on soft-magnetic properties, magnetoimpedance response, and field sensitivity in the nanocrystalline $(\text{Fe}_3\text{Ni})_{81}\text{Nb}_7\text{B}_{12}$ alloy ribbons. We observe that within the low-frequency regime, between 2 and 5 MHz, the zero-field-annealed (ZFA) ribbons exhibit the highest magnetoimpedance values. By magneto-optical Kerr effect measurements, we show that this result stems from the formation of irregular transversally patched magnetic domains after annealing, which in turn explains the induced transverse anisotropy necessary to increase the GMI response. In addition, we discuss this increment in terms of skin effect. Moreover, we report that the highest sensitivity of ca. 189%/(kA/m)—15%/Oe—is achieved for the field-annealed samples whose magnetic field was applied transverse to the ribbon axis. These findings are of practical importance to develop and refine highly sensitive magnetic sensors.

Keywords: magnetoimpedance effect; field sensitivity; domain structure; skin effect; FeNi-nanocrystalline ribbons



Citation: González-Alonso, D.; Gonzalez-Legarreta, L.; Marcin, J.; Švec, P.; Škorvánek, I. Tailoring Magnetic Properties and Magnetoimpedance Response in Nanocrystalline $(\text{Fe}_3\text{Ni})_{81}\text{Nb}_7\text{B}_{12}$ Ribbons for Sensor Applications. *Chemosensors* **2023**, *11*, 148. <https://doi.org/10.3390/chemosensors11020148>

Academic Editor: Jose V. Ros-Lis

Received: 23 December 2022

Revised: 24 January 2023

Accepted: 14 February 2023

Published: 17 February 2023



Copyright: © 2023 by the authors. Licensee MDPI, Basel, Switzerland. This article is an open access article distributed under the terms and conditions of the Creative Commons Attribution (CC BY) license (<https://creativecommons.org/licenses/by/4.0/>).

1. Introduction

The innumerable opportunities that soft-magnetic materials offer in everyday applications impel researchers to keep looking for new materials along with fine-tuning the existing ones. Soft-magnetic materials are especially suitable for high-performance power electronics [1], but their utilisation also involves static, low- and high-frequency applications [2]. Some of their widespread implementations includes transformers, generators and motors [3,4]. The basic utilisation of soft-magnetic materials consists in reducing energy loss from electrical appliances [5] and for sensing purposes [6]. The key defining characteristics of soft magnetic materials are low coercivity and high initial permeability. The latter feature in contrast to superparamagnetism [2,7]. Apart from eddy current losses, which is a limiting factor for high-frequency devices [5], coercivity stands for the energy devoted to reversing magnetic fields while obtaining complete demagnetisation of the material. Among soft-magnetic alloys, Fe-based amorphous-nanocrystalline materials stand out for their superior advantages as primarily concerned with economical, energy and environmental savings [2,4,5,8,9].

The discovery of a new family of compounds by Yoshizawa et al. in 1988—called FINEMET FeSiBNbCu —opened up new routes of investigation [10]. This new class of

materials displayed an excellent combination of soft-magnetic properties, including low coercivity, high permeability and near-zero magnetostriction, but with high saturation magnetisation up to 1.3 T. Similar soft-magnetic features were followed by the finding of two new families of compounds, i.e., NANOPERM FeZrBCu [11,12] and HITPERM (Fe,Co)–M–B–Cu, with M = [Zr, Nb, Hf, etc.] [13]. The underlying soft-magnetic behaviour in all the three aforementioned families stems from the ultrafine microstructure formation after a rapid solidification process followed by primary crystallization. In essence, the crystalline microstructure consists of single- or multiphase polycrystals embedded in the residual amorphous matrix after annealing [14]. The former crystalline microstructure comprises α /bcc-cubic of (Fe) and (Fe,Si) nanocrystals for both FINEMET and NANOPERM compounds. Nevertheless, HITPERM contains α /bcc-phases of (Fe) and (Fe,Co) nanocrystalline grains [13]. All of them reveal typical crystallite-sizes to range between 10 and 15 nm [14], which is well below the ferromagnetic exchange length [14,15]. Hence, they bear the name of nanocrystalline materials hereafter. The latter amorphous matrix contributes to their soft-magnetic behaviour. In fact, it was found that Cu and Nb elements, or other M elements belonging to groups IV–VI, act in favour of the formation of nanocrystalline grains by stabilising the amorphous matrix. These elements in turn hinder the emergence of borides while hampering the coarsening of bcc nanostructures [14,16]. It has been demonstrated that the Cu addition is not a necessary condition for the formation of ultrafine grain structures, which leads to the soft-magnetic behaviour in the FeNiNbB system [17,18] and/or in similar Fe(Ni)ZrB-based nanocrystalline alloys [19,20]. With the advent of nanocrystalline materials, originally found in ribbon shape, the need of global solutions for reducing energy costs coupled with the increasing demand for industrial applications has boosted the research of these materials.

After the works independently performed in non-magnetostrictive soft-magnetic amorphous wires by Panina and Mohri [21], and Beach and Berkovich [22,23], the giant magnetoimpedance (GMI) effect stands out among the properties of nanocrystalline materials for sensing purposes. Although according to M. Knobel and K.R. Pirota, the first study of magnetic-field dependence for the electrical impedance Z was reported about sixty years earlier in a Fe₂₂Ni₇₈ wire alloy [24], it was not until 1994 that a great effort was devoted to disclosing the mechanism behind the GMI effect due to their prospective implementation in a wide variety of applications [6,25]. Essentially, the GMI effect resides in the remarkable response of the complex ac impedance $Z = R_{dc} + j\omega L$ (R_{dc} , $\omega = 2\pi f$ and L represent the resistance, frequency and inductance, respectively) upon the application of an external magnetic field H_{dc} over a soft magnetic material with an ac current $I = I_0 e^{-j\omega t}$ (of known ω and I_0) flowing across [25]. Although GMI was originally studied in wires [21,23,24], it was extended over different geometries such as ribbons [26–28], microwires [29] and thin films [30]. By introducing the following relationship $\vec{B} = \mu\vec{H}$ into Maxwell equations, one obtains the ac impedance Z for an infinite planar film [31,32], which is close but not exact to a ribbon-shape:

$$Z = R_{dc} \cdot jka \cdot \coth(jka) \quad (1)$$

where R_{dc} is the dc electrical resistance of the ribbon, $2a$ is the thickness of the ribbon, $k = (1 - j)/\delta_m$ with j as the imaginary unit, and δ_m is the penetration or skin depth of the ribbon-shape magnetic material. The skin depth of a ribbon can be determined by the following expression [33]:

$$\delta_m = \frac{c}{\sqrt{4\pi^2 f \sigma \mu_T}} \quad (2)$$

where c is the speed of light, σ is the electrical conductivity, f is the frequency and μ_T is the transversal permeability of the ribbon.

It is noteworthy to mention that the GMI effect is very sensitive to the frequency f of the driving ac current flowing across the sample. Generally speaking, one can roughly establish

three different regimes for the GMI behaviour depending on the driving *ac* frequency *f*. In the very-low-frequency regime ($1 \leq f \leq 10$ kHz), the skin effect is negligible and the main contribution to the GMI comes from the magneto-inductance effect, i.e., the inductive voltage that is proportional to the transverse permeability. In the low-frequency regime ($10 \text{ kHz} \leq f \leq 10 \text{ MHz}$), the skin effect turns into dominant, and the MI response is caused by domain-wall motion and rotational magnetisation. For moderate frequencies ($10 \text{ MHz} \leq f \leq 1000 \text{ MHz}$), the domain-wall motion is strongly damped owing to eddy currents, and hence magnetic moment rotation turns into the driving force for the MI changes. At high frequencies—within the GHz range—important fluctuations of the penetration depth are observed, along with significant variations in the MI response, that are inferred to be consequences of ferromagnetic resonance [34]. This non-linear effect is indeed proved suitable to be exploited for sensor applications [35]. Furthermore, GMI-based magnetic sensors collect ideal characteristics such as low cost, miniaturisation, reduced noise and high magnetic field sensitivity to compete with conventional magnetic sensors, such as giant magnetoresistance magnetometers, fluxgate, and Hall effect, among others [36,37]. In contrast to sensitivities of ca. 12%/(kA/m)—1%/Oe—that are displayed by traditional magnetometers, based on the giant magnetoresistance effect, GMI sensors can achieve sensitivities as high as ca. 6000%/(kA/m)—500%/Oe [32].

In this work, we have conducted a comprehensive investigation in the nanocrystalline ribbon samples of nominal composition $(\text{Fe}_3\text{Ni})_{81}\text{Nb}_7\text{B}_{12}$ by connecting the induced magnetic anisotropy of the annealed ribbon samples—through the magnetic-domain structure observed by magneto-optical Kerr microscope measurements—with their soft-magnetic properties. In addition, we report the GMI response along with the magnetic field sensitivity of the set of annealed samples within the range $100 \text{ kHz} \leq f \leq 100 \text{ MHz}$ of the moderate frequencies, where rotational magnetisation drives the MI changes.

2. Materials and Methods

Amorphous ribbon samples with a nominal composition were prepared by the melting of pure elements better than 99.9% in an induction-melting furnace. Ribbons of 6 mm width and 20 μm thickness were obtained by a conventional planar flow casting method. The chemical composition and amorphous state of the as-cast ribbons was estimated by inductively coupled plasma spectroscopy and confirmed by X-ray diffraction (XRD), respectively. The sample presents a slightly positive magnetostriction coefficient [18], and the transverse magnetisation is expected to be due to pure rotation. In addition, the magnetostriction value is determined by the alloy composition but could be modified both by the fabrication process and suitable annealing [32,33]. The crystallisation temperatures of the as-cast ribbons were investigated using a differential scanning calorimeter (DSC) and a vibrating sample magnetometer (VSM). The DSC measurement was performed in a DSC 7 Perkin Elmer calorimeter at a constant heating rate of 10 K/min in the temperature range $340 \text{ K} \leq T \leq 970 \text{ K}$, whereas the temperature dependence of the magnetisation $M(T)$ was carried out in a MicroSense EV9 vibrating sample magnetometer (VSM) at a constant heating rate of 10 K/min with an external magnetic field of 80 kA/m—1 kOe—applied along the ribbon plane. Pieces of the as-cast ribbons of 60 mm length were selected to obtain nanocrystalline samples after heat treatments at 773 K for 1 h in a vacuum furnace to draw the influence of isothermal conventional annealing and isothermal field-annealing treatments on both the GMI effect and magnetic properties. Ribbons of 60 mm length have been selected to avoid undesirable demagnetisation effects while optimising the GMI effect [38,39]. Transversal (TFA) and longitudinal field-annealing (LFA) treatments were performed by applying a magnetic field strength of 640 kA/m perpendicular to the ribbon plane and 40 kA/m along the ribbon plane, respectively. In addition, as-cast and zero-field-annealed (ZFA) ribbons were employed as reference samples.

The structural analysis of the annealed ribbons was studied at room temperature in a Bruker D8 Advance with a Bragg–Brentano geometry and using Cu $K\alpha$ radiation $\lambda = 1.5418 \text{ \AA}$ with a graphite monochromator. The XRD pattern was recorded in the 2θ

range 20–105° with a resolution of 0.1°/step. Samples were mounted on a Si single-crystal low-background sample holder, which was rotated during data collection to reduce possible preferred orientation effects in the samples. The microstructure of the nanocrystalline samples was investigated at room temperature from the air-side of the ribbons by transmission electron microscopy (TEM) using a JEOL 2000FX microscope.

Room-temperature magnetic hysteresis-loops (HLs) were conducted along the ribbon axis under vacuum conditions by a high-temperature purpose-designed Förster-type B-H loop-tracer placed inside a magnetically shielded room. Magnetic-domain structures of the annealed ribbons were studied at room temperature from the air-side of the ribbons in a magneto-optical Kerr effect (MOKE) microscope of Evico Magnetics. Specimens for TEM analysis were polished by an Ar ion beam milling in PIPS using 4 kV/30 mA per ion gun.

Impedance measurements Z were carried out at room temperature with an Agilent 4294A impedance analyser using a 42941A standard probe. To measure the magnetoimpedance effect, all samples—as-cast and annealed ribbons—were placed within a long solenoid generating a homogeneous external dc magnetic field H_{dc} . The ac magnetic field perpendicular to the ribbon axis was produced by applying an alternating current flowing across the sample—i.e., driving ac current—with the typical constant rms value of 10 mA. The external magnetic field and the applied ac current are parallel to each other, and the working frequency range for the driving ac current lies within $100 \text{ kHz} \leq f \leq 100 \text{ MHz}$. The relative low value of the driving ac current has been selected to limit further undesirable non-linear effects, such as non-sinusoidal voltage and non-linear magnetisation reversal, which could result in additional treatments and/or in a reduction in the transversal magnetic field [22,32]. In addition, it was observed that for low values of the driving ac current, but high enough to overcome the transversal anisotropy—coercivity, the variation in the ac current produced both a clear change in the GMI and a lowering of the transverse anisotropy field [32,40]. A purpose-built sample holder was used to connect the ribbon samples by soldering them to the standard probe. To ensure the accuracy in the recorded data, a proper calibration of the 42941A standard probe and a sample holder compensation were both performed prior to every single measurement.

The MI response or GMI ratio $\Delta Z/Z(\%)$, whose Z -values are magnetic-field dependent, is defined as:

$$\left(\frac{\Delta Z}{Z}\right)(\%) = \left(\frac{Z(H) - Z(H_{max})}{Z(H_{max})}\right) \times 100\% \quad (3)$$

where $H_{max} = 10 \text{ kA/m}$ is the maximum dc magnetic field applied.

3. Results and Discussion

3.1. Structural and Magnetic Characterisation

Figure 1 is plotted to draw a comparison between the magnetisation $M(T)$ and DSC curves for the as-cast ribbon sample. The transition temperatures are collected in Table 1, where the temperatures for the magnetisation are determined from the minima points in the $dM(T)/dT$ curve, as shown in the inset of Figure 1a. Table 1 shows a good agreement of the transition temperatures obtained from both techniques.

Figure 1a displays the typical ferromagnetic (FM) behaviour below the Curie temperature T_C at about 540 K. This value of the Curie point is close to the ones reported in the literature for FeNi-based amorphous systems, in which the addition of small amounts of elements produces a rather smooth change in their Curie temperature [41,42]. This ferro-to-paramagnetic transition is revealed in the calorimetric measurement with a small bump at around 540 K, as indicated by a green-dashed line in Figure 1. Above T_C , the as-cast ribbon sample undergoes a second magnetic-phase transition as the temperature increases from the paramagnetic state (PM), as seen in Figure 1a. This second phase-transition is sensitive to the Ni content as reported for the $(\text{Fe}_{1-x}\text{Ni}_x)_{81}\text{Nb}_7\text{B}_{12}$ ribbon samples and results in a decrease in both their ferromagnetic-strength and their transition temperatures [17].

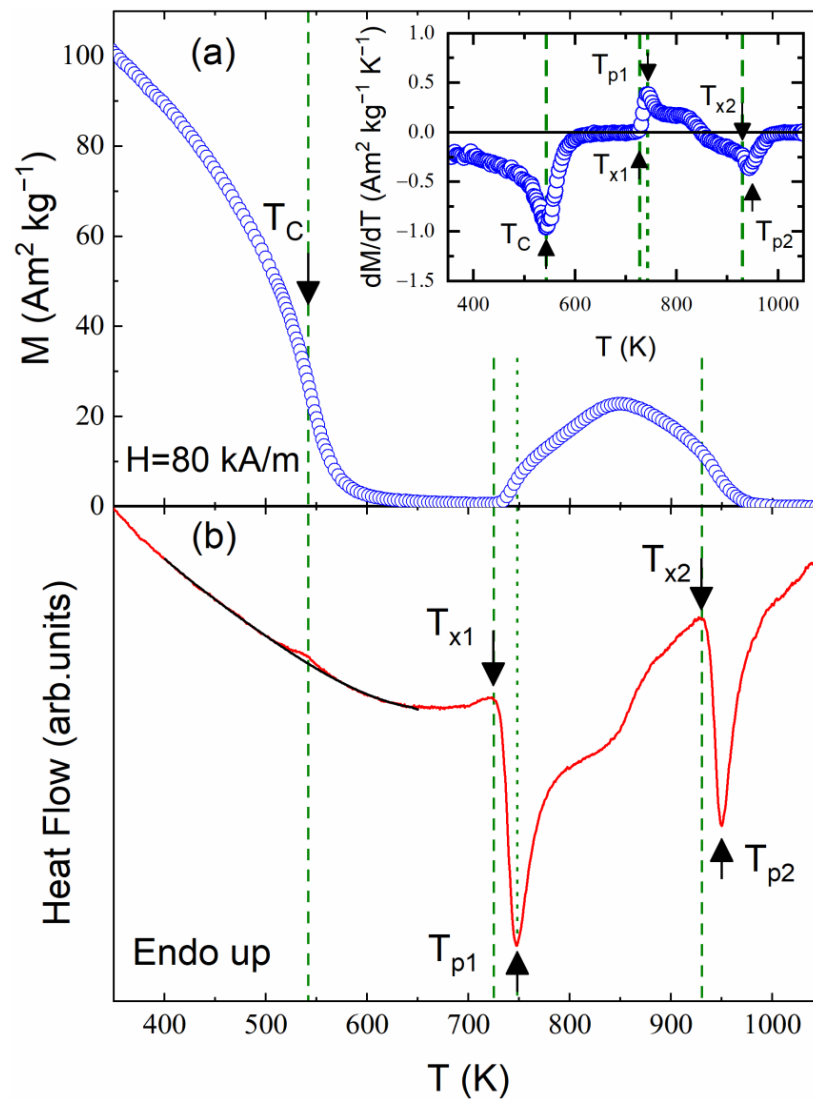


Figure 1. $M(T)$ (a) and DSC curves (b) of the as-cast $(\text{Fe}_3\text{Ni})_{81}\text{Nb}_7\text{B}_{12}$ ribbon sample, where T_C denotes the Curie point, T_{x1} (T_{p1}) and T_{x2} (T_{p2}) show the onset (peak/maximum) of the first and second crystallisation stages, respectively. The black line depicted in (b) indicates the baseline.

Table 1. Characteristic temperatures of the as-cast $(\text{Fe}_3\text{Ni})_{81}\text{Nb}_7\text{B}_{12}$ ribbon sample.

Technique	T_C (K)	T_{x1} (K)	T_{p1} (K)	T_{x2} (K)	T_{p2} (K)
M(T)	~543	~726	~741	~929	~944
DSC	~540	~728	~747	~936	~950

Investigations of the crystallisation of amorphous alloys are usually accompanied by DSC measurements at high enough heating-rates so that it intensifies the subtle features behind the transition [43,44]. Figure 1b depicts the formation of distinctive nanocrystalline phases for the as-cast $(\text{Fe}_3\text{Ni})_{81}\text{Nb}_7\text{B}_{12}$ amorphous ribbon by a DSC curve performed at a heating rate of 10 K/min. Two clearly different crystallisation stages are observed, which are very sensitive to the Ni content. In fact, a reduction in their crystallisation temperatures has been observed as the Ni content or the Fe/Ni ratio increase [18]. A similar behaviour was firstly reported by Kopcewicz et al. in a similar system with 20% Ni content [19]. The first crystallisation stage, though contentious, has been intensively studied [17–19,43–47]. During this primary crystallisation stage, the partial transformation from the amorphous to the α -/bcc-(Fe,Ni) phase together with a minimal fcc-(Fe,Ni) phase is broadly accepted.

The first to notice the bimodal behaviour of this stage was Suzuki et al. for a similar composition [43]. In view of this and regarding the $M(T)$ curve plotted in Figure 1a, the as-cast ribbon orders ferromagnetically at the onset of this primary crystallisation T_{x1} as the α -(Fe,Ni) nanograins are formed. Thus, the larger the amount of α -phase that is crystallised, the higher ferromagnetic ordering the sample presents. The second crystallisation stage is related to the formation of the fcc-(Fe,Ni)₂₃B₆ phase, which degenerates its good soft-magnetic features to the detriment of further applications [17,46].

Figure 2a shows the microstructure of the as-cast (Fe₃Ni)₈₁Nb₇B₁₂ ribbon sample after heat treatment at 773 K for 1 h. TEM micrographs of the air-side layer show ultrafine nanosized grains embedded in the residual amorphous matrix. The number-weighted mean value for the size of the nanograins was estimated by TEM measurements to range between 5 and 10 nm, which is well below the exchange correlation length [15].

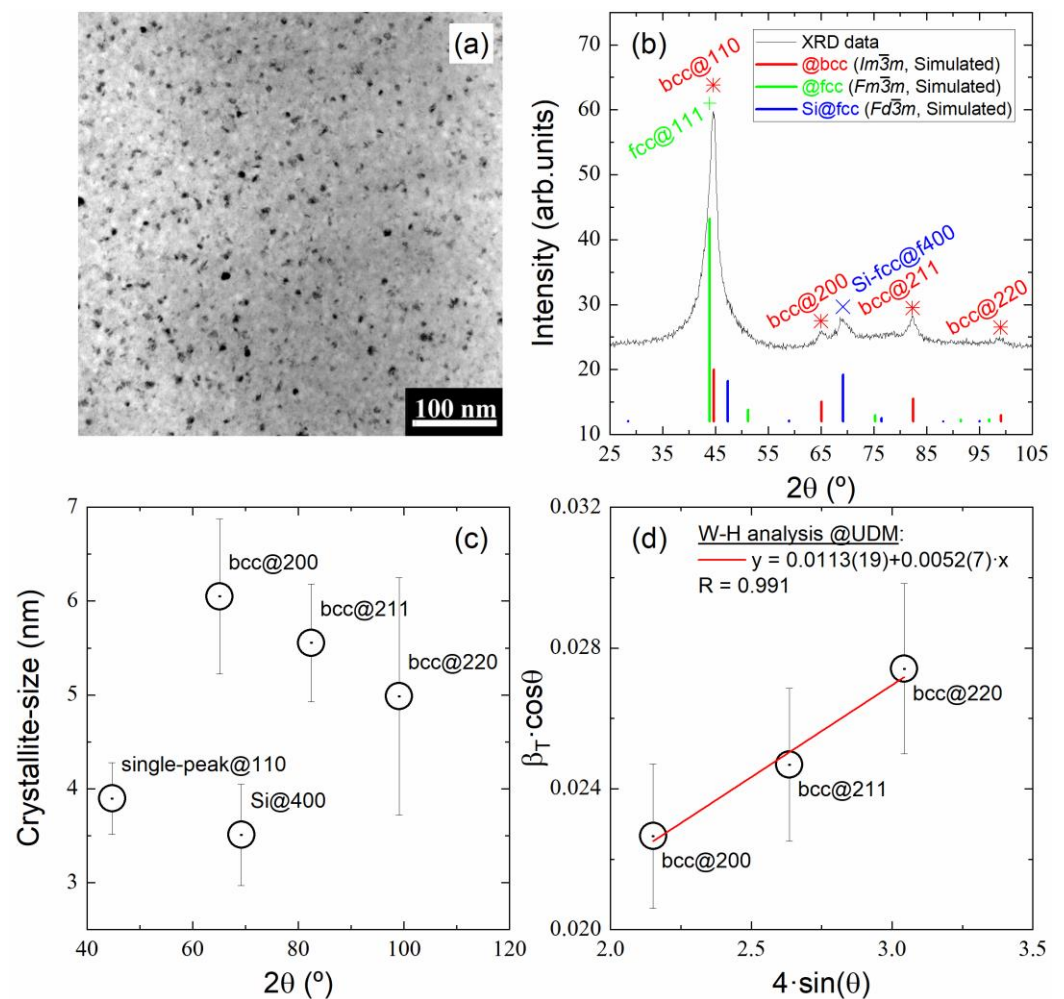


Figure 2. TEM micrograph showing the grains of the nanocrystalline (Fe₃Ni)₈₁Nb₇B₁₂ ribbon sample after annealing for 1 h at 773 K (a). The XRD pattern performed at room temperature (b). Crystallite-sizes obtained for the different diffraction peaks using the Scherrer equation (Equation (4)) (c) and the Williamson–Hall plot (d) of the nanocrystalline (Fe₃Ni)₈₁Nb₇B₁₂ ribbon sample annealed for 1 h at 773 K. Red, green and blue vertical lines shown in panel (b) are the simulated bcc-(Fe,Ni), fcc-(Fe,Ni), and fcc-Si phases, respectively. The simulated phases were performed thanks to FullProf [48] and using the crystallographic information collected in Table 2.

Table 2. Crystallographic information data [2,42,49].

Crystalline Phase	Crystal Structure	Lattice Parameter a (Å)	(hkl) Indexes
α -/bcc-(Fe,Ni)	$Im\bar{3}m$	$\sim 2.87 \pm 0.01$	110
γ -/fcc-(Fe,Ni)	$Fm\bar{3}m$	$\sim 3.59 \pm 0.01$	111
Si-fcc	$Fd\bar{3}m$	$\sim 5.43 \pm 0.01$	400

In order to fulfil the characterisation of the annealed ribbon samples, we have conducted a room-temperature XRD experiment to study the crystal structure of the as-cast ribbon after suitable annealing. Figure 2b shows the nanocrystalline XRD pattern of the as-cast sample after annealing. The XRD pattern of the as-cast sample has already been reported to be amorphous [18]. Diffraction peaks are ascribed to the typical cubic crystal structure [42] and revealed the coexistence of α -/bcc-(Fe,Ni) and γ -/fcc-(Fe,Ni) phases, as indicated in red and green, respectively, in Figure 2b. These reflections are indeed stemming from the crystallised nanograins embedded within the residual amorphous matrix after annealing, as seen in Figure 2a. The coexistence of these two phases at room temperature is expected for similar compositions of FeNi-based systems [41,42]. From visual inspection of Figure 2b, a bcc-(Fe,Ni) nanocrystalline phase appears to be preeminent. The reflection that appears at ca. 69.2° is assigned to the Si single-crystal low-background sample holder.

To determine the size of the nanograins from XRD data, we have employed different approaches. Firstly, the crystallite size determined for the largest single peak placed at around 45° lies around 4 ± 1 nm, as seen in Figure 2c, and was obtained by means of the Scherrer equation:

$$D_{Scherrer} = \frac{K \cdot \lambda_{Cu-k\alpha}}{\beta \cdot \cos\theta} \quad (4)$$

where K accounts for the crystallite-shape factor with the 0.89 value corresponding to a spherical shape, $\lambda_{Cu-k\alpha}$ is the X-ray wavelength of 1.5418 Å, β is the pure intensity breadth—without instrumental broadening—of a diffraction line or the angular Full-Width at Half-Maximum (FWHM) for a diffraction peak, and θ is the Bragg diffraction angle [50]. The crystallite size obtained for the nanograins using the FWHM at the largest peak is underestimated in comparison with the one obtained from TEM. This underrated value of the crystallite-grain size arises from the coexistence of the α - and γ -phases, which in turn results in an inflated measurement of the FWHM, as observed in Figure 2b. To correct this, we can fine-tune the approach by introducing strain considerations. In fact, Figure 2c shows the linear diminution of the crystallite size for the bcc-(Fe,Ni) peaks located at (200), (211) and (220) reflections as the Bragg angle increases. Thus, analysing these three peaks by means of the Williamson–Hall method, and assuming a uniform deformation model [51,52], we can separate both the crystallite-size $\beta_{Scherrer}$ and the lattice strain β_ϵ contributions from the line broadening as follows:

$$\begin{aligned} \beta_{Total} \cdot \cos\theta &= (\beta_{Scherrer} + \beta_\epsilon) \cdot \cos\theta = \\ &= \frac{K_{sphere} \cdot \lambda_{Cu-k\alpha}}{D} + 4 \cdot \langle \epsilon \rangle \cdot \sin\theta \end{aligned} \quad (5)$$

where $\langle \epsilon \rangle$ is the mean value of the microstrain that it is assumed to be uniform. By this approach, we obtain a crystallite size of 12 ± 2 nm and a mean microstrain of $52 \pm 7 \times 10^{-4}$, as observed in the Williamson–Hall plot shown in Figure 2d. Therefore, the crystallite sizes of the nanograins of the bcc-(Fe,Ni) phase determined by both TEM and XRD data are in very good agreement.

3.2. Magnetic Behaviour

Figure 3a shows the HLs of the as-cast, ZFA, TFA, and LFA annealed ribbons. Typical soft-magnetic materials are characterised by very low coercive fields H_C , as seen in the inset of Figure 3a and in Figure 3b [5,26,53]. Indeed, the coercivity reduction with respect

to the increment of Ni content for the $(\text{Fe}_{1-x}\text{Ni}_x)_{81}\text{Nb}_7\text{B}$ samples annealed at 773 K was already reported by Turčanová et al. [17]. As expected, the LFA sample exhibits the softest magnetic properties with a coercivity of 7 A/m. However, ZFA and TFA samples show a deterioration in their coercivity with respect to the as-cast one. This is due to the directional ordering of atomic pairs mechanism [54,55]. The lowering in the coercive field after LFA has already been noticed in several other soft-magnetic nanocrystalline systems [56–58] and can be described by the formation of magnetic-domain structures preferentially oriented along the ribbon axis, which enhances magnetisation processes brought about by the 180° domain-wall motion occurring at lower fields [56,59]. Panels (c–e) of Figure 3 show the different magnetic-domain structures obtained by MOKE for all the annealing samples. The ZFA ribbons exhibit a tendency to form irregular transversally patched magnetic domains as seen in Figure 3c, whereas the LFA and TFA samples show the presence of wide magnetic domains aligned in longitudinal and transversal directions, respectively, as expected.

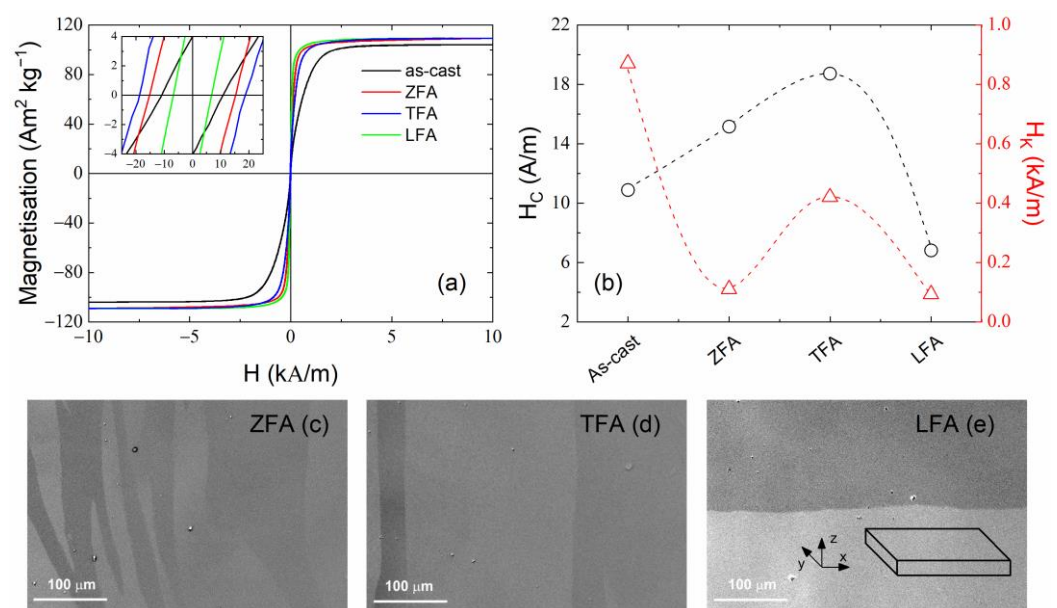


Figure 3. Axial hysteresis loops performed at room temperature for different annealed treatments of the $(\text{Fe}_3\text{Ni})_{81}\text{Nb}_7\text{B}_{12}$ ribbon sample (a). Inset in panel (a) shows a magnification of HLs to visualise the coercive fields H_C . Variation of coercivity and effective magnetic anisotropy—obtained from HLs—for the different annealing treatments (b). Panels (c–e) show the magnetic-domain structure performed at room temperature by MOKE for the different annealed ribbon samples. The sketch displayed in panel (e) is a guidance of the magnetic domain structure with respect to the ribbon.

Conventional annealing is expected to produce a magnetic hardening, together with an increment in the saturation magnetisation, as seen in Figure 3a,b. The enhancement of the saturation magnetisation is explained for all the annealed samples studied here in terms of the crystallisation of the ferromagnetic bcc-(Fe,Ni) phase [32,40]. Furthermore, the HL of the TFA ribbons displays a slightly lower slope of the loop branches in comparison with the LFA ribbons, as seen in the magnetisation kink of Figure 3a. This reduction—in the TFA susceptibility χ_{TFA} —is indicative of the formation of an induced magnetic anisotropy along the transverse direction of the TFA ribbons, as observed in Figure 3d. Such type of soft-magnetic behaviour shown in the HLs is of special interest for sensor applications, whereas the reduced susceptibility makes them suitable for high-frequency transformer applications [1,8,60].

3.3. Magnetoimpedance Response

To pinpoint the effects of field annealing on the MI response, a detailed study of the frequency and magnetic-field dependence has been performed. Figure 4 gathers the

magnetic-field dependence of the MI response for the set of as-cast and field-annealed $(\text{Fe}_3\text{Ni})_{81}\text{Nb}_7\text{B}_{12}$ ribbon samples studied in this work. In all cases, both the external *dc* magnetic field and the driving *ac* current were applied along the ribbon-axis direction at the selected frequencies. Within this intermediate frequency regime, it has been reported that for small ferromagnetic conductors such as ribbon samples, the magnetisation rotation is the main contribution to the GMI effect. This is because at high enough frequencies, the domain wall motion is strongly damped due to eddy currents formation, and therefore, its contribution can be neglected [32,40,61].

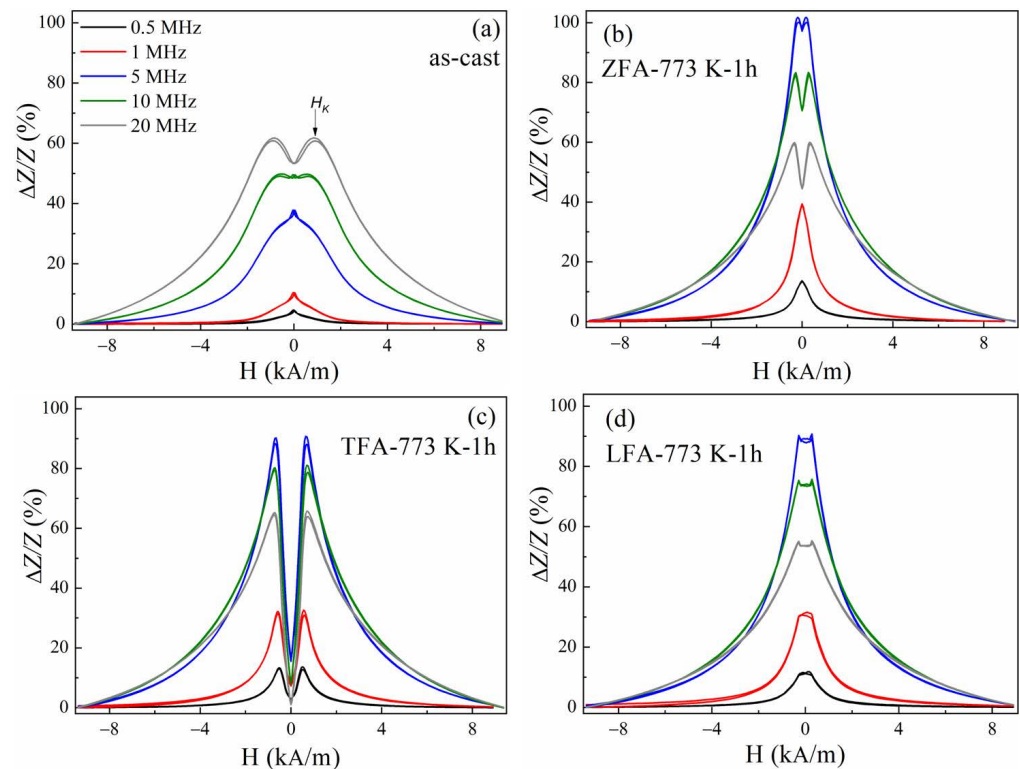


Figure 4. Magnetoimpedance effect of as-cast (a), ZFA (b), TFA (c) and LFA (d) for $(\text{Fe}_3\text{Ni})_{81}\text{Nb}_7\text{B}_{12}$ ribbon calculated by Equation (3).

In Figure 4a, the as-cast sample shows a single-peak feature at frequencies below 5 MHz. However, the two-peak behaviour emerges for increasing frequencies. There should be noticed a three-peaks demeanour that appears at intermediate frequencies between 5 and 20 MHz. This intermediate feature should be associated with the gradual evolution from single-to-two-peak behaviour. In general, the single-to-two-peak evolution depends on the effective magnetic anisotropy undergone within the sample [25,31,32]. In this regard, a longitudinal magnetic anisotropy—magnetic easy-axis along the ribbon axis—with respect to both the external *dc* magnetic field and the *ac* current is a requirement for the single-peak feature. By contrast, the double-peak structure requires a transversal magnetic anisotropy with respect to both *ac* current and external applied *dc* field, which are indeed parallel to each other [32,40]. Therefore, thermal treatments—among other types of annealing such as stress [62] or torsion annealing—are used to induce transverse magnetic anisotropy at the expense of the intrinsic magnetic anisotropies originated during the fabrication process. Thus, the two-peak behaviour is obtained, which could be relevant for its interesting applications [40]. In this respect, Figure 4b–d show the MI response for a varied scenario concerning the different anisotropies induced after field annealing. The ZFA ribbon sample exhibits the typical MI response for materials with single-to-two-peak evolution, as expected from the characteristic magnetic-domain structure displayed in Figure 3c. This phenomenon can be explained through the imbalance between longitudinal and transverse magnetic anisotropies produced for increasing frequencies. It is worth

mentioning that both the transverse magnetic anisotropy and switching field—the necessary field to overcome rotational magnetisation—increase as the frequency rises, which in turn causes the single-to-two-peak demeanour in the MI response [27].

In Figure 4c, the TFA ribbon sample exhibits the two-peak behaviour in the entire frequency range due to the dominant transverse magnetic anisotropy induced during the field-annealing treatment, as seen in Figure 3d. Finally, the LFA ribbon sample shows a less defined single-peak feature derived from the dominant longitudinal magnetic anisotropy for the whole studied frequency range [40]. Thus, ZFA, TFA and LFA samples show diverse MI responses that can be explained as a result of the different effective magnetic anisotropies induced during annealing, as observed in the MOKE pictures displayed in Figure 3c–e. Furthermore, only the ZFA and the as-cast samples undergo the single-to-two-peak evolution as the frequency increases. The former takes place above 1 MHz, whereas the latter takes place above 10 MHz, as seen in Figure 4a,b, respectively. We surmise that the larger frequency of 10 MHz is required for the two-peak structure in the as-cast sample—to enhance the transversal permeability or transverse magnetic anisotropy—because of the large internal stresses induced during the fabrication process. In addition, the maximum GMI ratio for the two-peak behaviour is reached at higher dc applied fields—anisotropy field H_K —for the as-cast sample. In sum, the GMI response can be improved by relaxing internal stresses through thermal treatments—ZFA, but it can also be enhanced by inducing anisotropies during the annealing at suitable temperatures by field—TFA and LFA—or stress annealing [29,62].

With regard to the effect of field annealing on the GMI response, shown in Figure 5a, we draw a comparison between as-cast and annealed samples for the GMI ratio $\Delta Z/Z(H, f)$ at 5 MHz. There, we confirm the dissimilar effect of the different annealing treatments on the GMI response. It is clearly appreciated that there is a significant GMI improvement for all the annealed ribbon samples when compared to the as-cast sample. In fact, all the annealed samples show an increase in the GMI ratio above 90% at 5 MHz, whereas for the as-cast sample, it lies around 35%. The largest $\Delta Z/Z(\%)$ ratio value increased up to ca. 100% for the ZFA ribbon sample. By contrast, the double-peak behaviour appears with a more pronounced dip at zero field for the TFA sample, as seen in Figure 4c. This is because the TFA sample exhibits the highest effective anisotropy field H_K among the annealed samples, as shown in Figure 3b and/or in Figure 4, in which internal stresses were reduced after suitable annealing when comparing the as-cast sample. Therefore, conventional field-annealing is revealed as an adequate treatment to improve the GMI response.

At relative low frequencies—for the quasistatic model, it is broadly accepted that the driving ac current flows across the whole ferromagnetic ribbon—i.e., the skin depth is comparable to the ribbon thickness $\delta_m \approx 2a$ [40]. At increasing frequencies, however, the effective area through which the driving ac current flows decreases and is accompanied by an induced transverse magnetic anisotropy near the ribbon surface $\delta_m \lesssim a$. In this situation, the skin effect starts to become relevant for the description of the MI response. As will be shown below, this scenario corresponds to the frequency range studied for all samples. Consequently, the skin depth δ_m has been calculated using the following simple relationship for ribbon samples [63]:

$$\delta_m = a \frac{R_{dc}}{R_{ac}} \quad (6)$$

where $2a$ is the ribbon thickness, and R_{dc} and R_{ac} denote the dc and ac resistance at a given frequency of the driving ac current. To show the variation of the skin depth with respect to the frequency, it is defined as follows: $\Delta\delta_m = \delta_m(H_{max,dc} = 10\text{kA/m}) - \delta_m(H_{dc} = 0)$ [64].

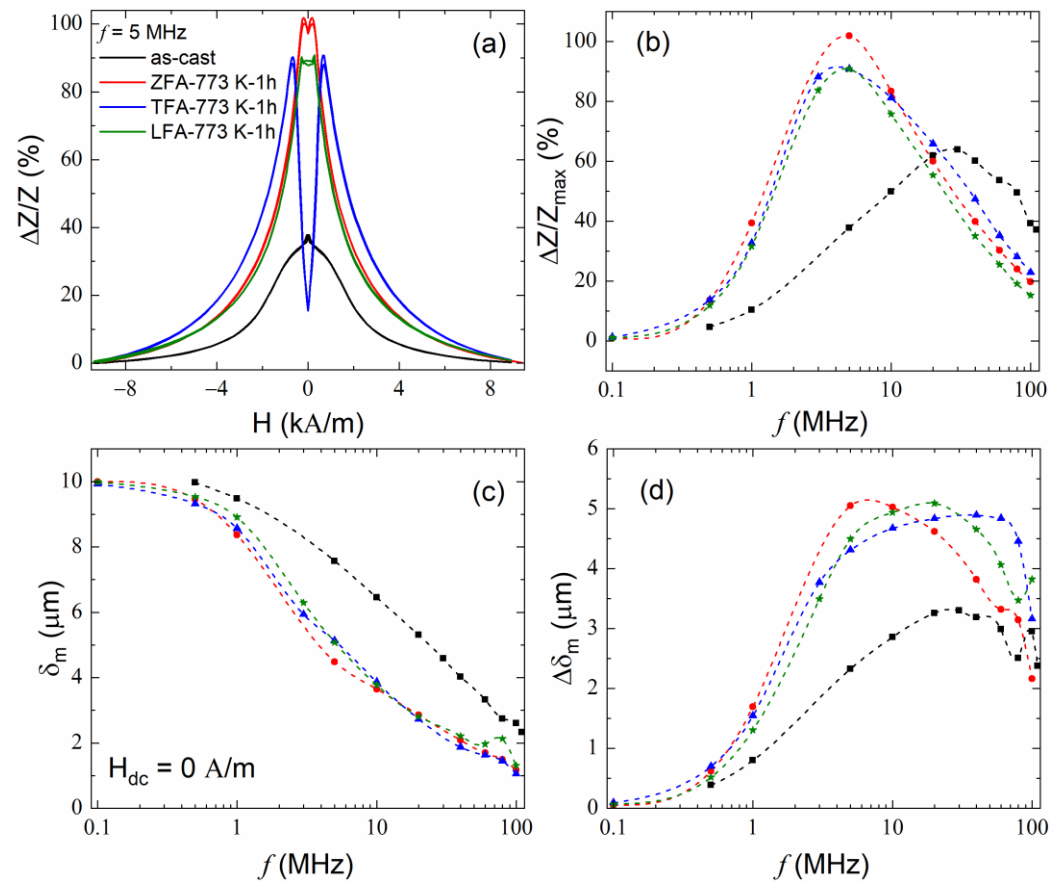


Figure 5. Magnetic-field dependence of the MI response for the as-cast and annealed $(\text{Fe}_3\text{Ni})_{81}\text{Nb}_7\text{B}_{12}$ ribbon samples (a), in which the driving frequency is equal to 5 MHz. Panel (b) shows the frequency dependence of the maximum MI response ($\Delta Z/Z_{\text{max}}$ (%)). Panel (c) shows the frequency dependence of the calculated skin depth δ_m , and panel (d) displays the variation of the skin depth $\Delta\delta_m = \delta_m(H_{\text{max},\text{dc}} = 10 \text{ kA/m}) - \delta_m(H_{\text{dc}} = 0)$ for all samples. In panels (b–d), symbols denote the experimental data, whereas the dashed lines are guides to the eye.

In Figure 5b, it is observed that for all the annealed samples, the MI response $\Delta Z/Z$ (%) increases monotonously up to ca. 5 MHz, and then it starts to diminish. For the as-cast sample, however, this maximum is shifted towards higher frequencies. This reduction in the MI response agrees with the largest variation observed for the skin depth concurring above the same characteristic frequency threshold, as seen in Figure 5c,d. Above this frequency threshold, it is observed that all the annealed samples experience a decrease in their MI response. We surmise this detriment stems from other unconsidered effects, such as non-linear effects, that may be taking place.

Finally, we show the field sensitivity η for all ribbons, since it allows to discriminate on grounds of performing among magnetic sensors and could be used to determine the best treatment. To calculate η , the following expression has been employed:

$$\eta = \frac{\partial(\Delta Z/Z)}{\partial H} \quad (7)$$

Figure 6 shows the frequency and field dependence of the field sensitivity. Except for the TFA sample, the field sensitivity displays minor differences in the frequency dependence among samples. Particularly, the TFA ribbons can reach field sensitivities as high as 200%/(kA/m) in the field range 225–575 A/m at 3 MHz. This field-sensitivity value is larger than previous reported values in Fe systems [65,66]. In addition, in Figure 5a, it is observed that the maximum field sensitivity is reduced from 80 MHz for the as-cast sample

to the frequency range of 1–5 MHz for the annealed samples. We surmise this effect is a consequence of the induced magnetic-domain structures along with the magnetoelastic anisotropy increment in the annealed ribbon samples. Therefore, the positive effect of the field annealing on field sensitivity is noticed here, and it is specifically enhanced by TFA. Moreover, the frequency range in which the field sensitivity is enhanced is optimal for sensor purposes because of their large signal-to-noise ratio, that is, without expensive post-processing costs [67]. In summary, field annealing arises here as a suitable technique to simultaneously enhance the GMI ratio and field sensitivity.

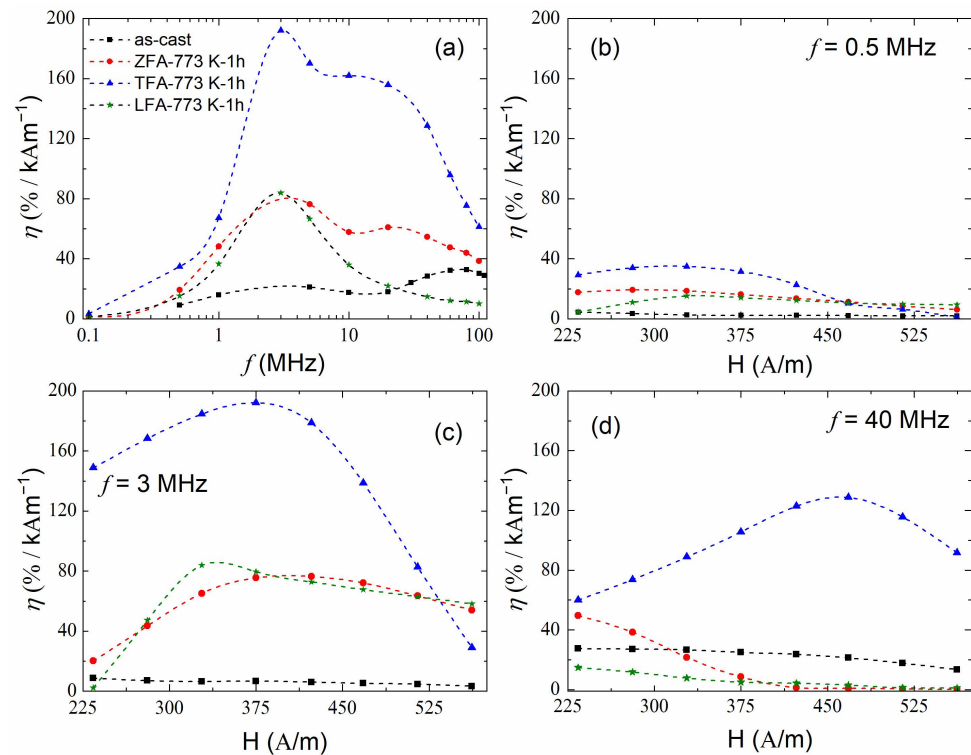


Figure 6. Frequency dependence of the field sensitivity η (% / (kAm⁻¹)) determined by Equation (7) for all ribbon samples (a). Panels (b–d) show the magnetic field dependence of the sensitivity at selected frequencies for all studied ribbon samples. In panels (b–d), symbols denote the experimental data, whereas dashed lines are guides to the eye.

4. Conclusions

In this work, we have conducted a comprehensive investigation to study the magnetic properties, magnetoimpedance response and field sensitivity of as-cast and field-annealed nanocrystalline (Fe₃Ni)₈₁Nb₇B₁₂ ribbon samples. We determined the suitability of field annealing to enhance both the GMI ratio and field sensitivity for these alloys. The GMI ratio and field-sensitivity values increased from about 63% at 30 MHz and 33% / (kAm⁻¹) at 80 MHz for the as-cast sample, respectively, to about 102% at 5 MHz for the GMI ratio of the ZFA sample and 193% / (kA/m) at 3 MHz for the field sensitivity of the TFA sample. The analysis conducted in this work shows that both MI response and field sensitivity are responsive to modifications in the magnetic anisotropy and/or skin depth by means of—field mediated or not—heat treatments. In light of these, we conclude that the larger transversal-magnetic anisotropy is induced via field annealing, the lower characteristic frequency at which the MI response $\Delta Z/Z$ (%) reaches its maximum. This is indicative of the benefits that field annealing offers to low-frequency applications, i.e., between 2 and 5 MHz. In summary, applying suitable field-annealing treatments towards nanocrystalline Fe-Ni-Nb-B alloy ribbons allows the design of attractive components for their usage in low- and intermediate-frequency magnetic sensors.

Author Contributions: D.G.-A. and L.G.-L. writing—original draft preparation; D.G.-A. and L.G.-L. writing—review and editing the manuscript; P.Š. prepared the samples and performed XRD and TEM experiments; L.G.-L. and J.M. performed the magnetic and GMI measurements; I.Š. performed domain structure observation by MOKE; D.G.-A. and L.G.-L. participated in the result analysis; D.G.-A., L.G.-L., P.Š. and I.Š. participated in the discussion; I.Š. funding acquisition. All authors have read and agreed to the published version of the manuscript.

Funding: This research was funded by the projects APVV-19-0369 and VEGA 2/0148/23.

Institutional Review Board Statement: Not applicable.

Data Availability Statement: The data that support the findings of this study are available from the corresponding author upon reasonable request.

Acknowledgments: D.G.-A. and L.G.-L. acknowledge the support of the National Scholarship Program of the Slovak Republic awarded in the academic year 2014-15.

Conflicts of Interest: The authors declare no conflict of interest.

References

1. Leary, A.M.; Ohodnicki, P.R.; McHe, M.E. Soft Magnetic Materials in High-Frequency, High-Power Conversion Applications. *JOM* **2012**, *64*, 772–781. [[CrossRef](#)]
2. Coey, J.M.D. *Magnetism and Magnetic Materials*, 1st ed.; Cambridge University Press: Cambridge, UK, 2010.
3. Silveyra, J.M.; Ferrara, E.; Huber, D.L.; Monson, T.C. Soft magnetic materials for a sustainable and electrified world. *Science* **2018**, *362*, eaao0195. [[CrossRef](#)] [[PubMed](#)]
4. Gutfleisch, O.; Willard, M.A.; Brück, E.; Chen, C.H.; Sankar, S.G.; Ping Liu, J. Magnetic Materials and Devices for the 21st Century: Stronger, Lighter, and More Energy Efficient. *Adv. Mater.* **2011**, *23*, 821–842. [[CrossRef](#)]
5. Herzer, G. Modern soft magnets: Amorphous and nanocrystalline materials. *Acta Mater.* **2013**, *61*, 718–734. [[CrossRef](#)]
6. Jiles, D. Recent advances and future directions in magnetic materials. *Acta Mater.* **2003**, *51*, 5907–5939. [[CrossRef](#)]
7. Luborsky, F.E. Development of Elongated Particle Magnets. *J. Appl. Phys.* **1961**, *32*, 171S–183S. [[CrossRef](#)]
8. Zhou, J.; You, J.; Qiu, K. Advances in Fe-based amorphous/nanocrystalline. *J. Appl. Phys.* **2022**, *132*, 040702. [[CrossRef](#)]
9. Li, H.; Wang, A.; Liu, T.; Chen, P.; He, A.; Li, Q.; Luan, J.; Liu, C.-T. Design of Fe-based nanocrystalline alloys with superior magnetization and manufacturability. *Mater. Today* **2021**, *42*, 49–56. [[CrossRef](#)]
10. Yoshizawa, Y.; Oguma, S.; Yamauchi, K. New Fe-based soft magnetic alloys composed of ultrafine grain structure. *J. Appl. Phys.* **1988**, *64*, 6044–6046. [[CrossRef](#)]
11. Suzuki, K.; Kataoka, N.; Inoue, A.; Makino, A.; Masumoto, T. High Saturation Magnetization and Soft Magnetic Properties of bcc Fe–Zr–B Alloys with Ultrafine Grain Structure. *Mater. Trans. JIM* **1990**, *31*, 743–746. [[CrossRef](#)]
12. Makino, A.; Inoue, A.; Masumoto, T. Nanocrystalline Soft Magnetic Fe–M–B (M=Zr, Hf, Nb) Alloys Produced by Crystallization of Amorphous Phase. *Mater. Trans. JIM* **1995**, *36*, 924–938. [[CrossRef](#)]
13. Willard, M.A.; Laughlin, D.E.; McHenry, M.E. Structure and magnetic properties of (Fe_{0.5}Co_{0.5})₈₈Zr₇B₄Cu₁ nanocrystalline alloys. *J. Appl. Phys.* **1998**, *84*, 6773–6777. [[CrossRef](#)]
14. Herzer, G. Nanocrystalline soft magnetic materials. *Phys. Scr.* **1993**, *T49*, 307–314. [[CrossRef](#)]
15. Herzer, G. Grain size dependence of coercivity and permeability in nanocrystalline ferromagnets. *IEEE Trans. Magn.* **1990**, *26*, 1397–1402. [[CrossRef](#)]
16. Hono, K.; Hiraga, K.; Wang, Q.; Inoue, A.; Sakurai, T. The microstructure evolution of a Fe_{73.5}Si_{13.5}B₉Nb₃Cu₁ nanocrystalline soft magnetic material. *Acta Metall. Mater.* **1992**, *40*, 2137–2147. [[CrossRef](#)]
17. Turčanová, J.; Marcin, J.; Kováč, J.; Janičkovič, D.; Švec, P.; Škorvánek, I. Magnetic and Mechanical Properties of Nanocrystalline Fe–Ni–Nb–B Alloys. *J. Phys. Conf. Ser.* **2009**, *144*, 012065. [[CrossRef](#)]
18. Švec, P.; Miglierini, M.; Dekan, J.; Turčanová, J.; Vlasák, G.; Škorvánek, I.; Janičkovič, D.; Švec, S.P. Influence of Structure Evolution on Magnetic Properties of Fe–Ni–Nb–B System. *IEEE Trans. Magn.* **2010**, *46*, 412–415. [[CrossRef](#)]
19. Kopcewicz, M.; Idzikowski, B.; Kalinowska, J. Mössbauer study of the magnetism and structure of amorphous and nanocrystalline Fe_{81–x}Ni_xZr₇B₁₂ (x = 10–40) alloys. *J. Appl. Phys.* **2003**, *94*, 638–649. [[CrossRef](#)]
20. Kopcewicz, M.; Grabias, A.; Nowicki, P.; Williamson, D.L. Mössbauer and x-ray study of the structure and magnetic properties of amorphous and nanocrystalline Fe₈₁Zr₇B₁₂ and Fe₇₉Zr₇B₁₂Cu₂ alloys. *J. Appl. Phys.* **1996**, *79*, 993–1003. [[CrossRef](#)]
21. Panina, L.V.; Mohri, K. Magneto-impedance effect in amorphous wires. *Appl. Phys. Lett.* **1994**, *65*, 1189–1191. [[CrossRef](#)]
22. Beach, R.S.; Berkowitz, A.E. Giant magnetic field dependent impedance of amorphous FeCoSiB wire. *Appl. Phys. Lett.* **1994**, *64*, 3652–3654. [[CrossRef](#)]
23. Beach, R.S.; Berkowitz, A.E. Sensitive field- and frequency-dependent impedance spectra of amorphous FeCoSiB wire and ribbon. *J. Appl. Phys.* **1994**, *76*, 6209–6213. [[CrossRef](#)]
24. Harrison, E.P.; Turney, G.L.; Rowe, H.; Gollop, H. The Electrical Properties of High Permeability Wires Carrying Alternating Current. *Proc. R. Soc. A* **1936**, *157*, 451–479.

25. Knobel, M.; Pirota, K. Giant magnetoimpedance: Concepts and recent progress. *J. Magn. Magn. Mater.* **2002**, *242–245*, 33–40. [[CrossRef](#)]
26. González-Legarreta, L.; Andrejka, F.; Marcin, J.; Švec, P.; Varga, M.; Janičkovič, D.; Švec, S.P.; Škorvánek, I. Magnetoimpedance effect in nanocrystalline Fe_{73.5}Cu₁Nb₃Si_{13.5}B₉ single-layer and bilayer ribbons. *J. Alloys Comp.* **2016**, *688*, 94–100. [[CrossRef](#)]
27. Phan, M.-H.; Peng, H.-X.; Wisnom, M.R.; Yu, S.-C. Giant magnetoimpedance effect in ultrasoft FeAlSiBCuNb nanocomposites for sensor applications. *J. Appl. Phys.* **2005**, *98*, 1–7. [[CrossRef](#)]
28. Vega, V.; Prida, V.; Hernando, B.; Ipatov, M.; Chizhik, A.; Zhukova, V.; Zhukov, A.; Domínguez, L.; González, J. Improvement of high frequency giant magnetoimpedance effect in CoFeSiB amorphous ribbon with vanishing magnetostriction by electrodeposited Co coating surface layer. *J. Mater. Res. Technol.* **2021**, *15*, 6929–6939. [[CrossRef](#)]
29. González-Alonso, D.; González-Legarreta, L.; Corte-León, P.; Zhukova, V.; Ipatov, M.; Blanco, J.M.; Zhukov, A. Magnetoimpedance Response and Field Sensitivity in Stress-Annealed Co-Based Microwires for Sensor Applications. *Sensors* **2020**, *20*, 3227. [[CrossRef](#)]
30. García, D.; Muñoz, J.; Kurllyandskaya, G.; Vázquez, M.; Ali, M.; Gibbs, M. Induced anisotropy, magnetic domain structure and magnetoimpedance effect in CoFeB amorphous thin films. *J. Magn. Magn. Mater.* **1999**, *191*, 339–344. [[CrossRef](#)]
31. Kraus, L. Theory of giant magneto-impedance in the planar conductor with uniaxial magnetic anisotropy. *J. Magn. Magn. Mater.* **1999**, *195*, 764–778. [[CrossRef](#)]
32. Phan, M.-H.; Peng, H.-X. Giant magnetoimpedance materials: Fundamentals and applications. *Prog. Mater. Sci.* **2008**, *53*, 323–420. [[CrossRef](#)]
33. Panina, L.; Mohri, K.; Uchiyama, T.; Noda, M.; Bushida, K. Giant magneto-impedance in Co-rich amorphous wires and films. *IEEE Trans. Magn.* **1995**, *31*, 1249–1260. [[CrossRef](#)]
34. Yelon, A.; Ménard, D.; Britel, M.; Ciureanu, P. Calculations of giant magnetoimpedance and of ferromagnetic resonance response are rigorously equivalent. *Appl. Phys. Lett.* **1996**, *69*, 3084–3085. [[CrossRef](#)]
35. Kurllyandskaya, G.V.; Lezama, L.; Pasynkova, A.A.; Volchkov, S.O.; Lukshina, V.A.; Larrañaga, A.; Dmitrieva, N.V.; Timofeeva, A.V.; Orue, I. Amorphous FeCoCrSiB Ribbons with Tailored Anisotropy for the Development of Magnetic Elements for High Frequency Applications. *Materials* **2022**, *15*, 4160. [[CrossRef](#)] [[PubMed](#)]
36. Ding, L.; Saez, S.; Dolabdjian, C.; Melo, L.G.C.; Yelon, A.; Menard, D. Equivalent Magnetic Noise Limit of Low-Cost GMI Magnetometer. *IEEE Sens. J.* **2009**, *9*, 159–168. [[CrossRef](#)]
37. Zhukov, A.; Ipatov, M.; Churyukanova, M.; Talaat, A.; Blanco Zhukova, V. Trends in optimization of giant magnetoimpedance effect in amorphous and nanocrystalline materials. *J. Alloys Comp.* **2017**, *727*, 887–901. [[CrossRef](#)]
38. Qin, H.; Yu, X.; Li, B.; Hao, Y.; Huang, S.; Hu, J.; Jiang, M. Sample Length Dependence of Giant Magnetoimpedance in Fe–Zr–Nb–Cu–B Nanocrystalline Ribbons. *Mater. Trans. JIM* **2005**, *46*, 1261–1263. [[CrossRef](#)]
39. Chaturvedi, A.; Dhakal, T.P.; Witanachchi, S.; Le, A.-T.; Phan, M.-H.; Srikanth, H. Critical length and giant magnetoimpedance in Co₆₉Fe_{4.5}Ni_{1.5}Si₁₀B₁₅ amorphous ribbons. *Mater. Sci. Eng. B* **2010**, *172*, 146–150. [[CrossRef](#)]
40. Knobel, M.; Vázquez, M.; Kraus, L. Giant Magnetoimpedance. In *Handbook of Magnetic Materials*, 1st ed.; Buschow, K., Ed.; Elsevier: Amsterdam, The Netherlands, 2003; Volume 15.
41. Chikazumi, S.; Graham, C. *Physics of Ferromagnetism*, 2nd ed.; Oxford University Press: Oxford, UK, 1999; pp. 241–243.
42. Bozorth, R.M. *Ferromagnetism*; IEEE Press: Piscataway, NJ, USA, 1993; p. 102.
43. Suzuki, K.; Cadogan, J.M.; Dunlop, J.B.; Sahajwalla, V. Two stage nanostructural formation process in Fe–Nb–B soft magnetic alloys. *Appl. Phys. Lett.* **1995**, *67*, 1369–1371. [[CrossRef](#)]
44. Kolano-Burian, A.; Kowalczyk, M.; Grabias, A.; Radoń, A.; Blyskun, P.; Warski, T.; Karpiński, M.; Hawelek, L.; Kulik, T. The influence of ultra-rapid annealing on nanocrystallization and magnetic properties of Fe_{76-x}Ni₁₀B₁₄Cu_x alloys. *J. Alloys Comp.* **2022**, *921*, 165943. [[CrossRef](#)]
45. Chen, Z.; Kang, S.; Zhu, Q.; Zhang, K.; Hu, J.; Jiang, Y. Effect of Fe/Ni ratio on amorphization, crystallization kinetics, and magnetic properties of FeNiSiBCuNb alloys. *J. Non Cryst. Solids* **2022**, *595*, 121842. [[CrossRef](#)]
46. Švec, P.; Švec Sr, P.; Hosko, J.; Janickovic, D. Formation of monophasic Fe₂₃B₆-type alloy via crystallization of amorphous Fe–Ni–Nb–B system. *J. Alloys Comp.* **2014**, *590*, 87–91. [[CrossRef](#)]
47. Suzuki, K.; Parsons, R.; Zang, B.; Onodera, K.; Kis, H.; Kato, A. Copper-free nanocrystalline soft magnetic materials with high saturation magnetization comparable to that of Si steel. *Appl. Phys. Lett.* **2017**, *110*, 012407. [[CrossRef](#)]
48. Rodríguez-Carvajal, J. Recent advances in magnetic structure determination by neutron powder diffraction. *Phys. B* **1993**, *192*, 55–69. [[CrossRef](#)]
49. Hubbard, C.R.; Swanson, H.E.; Mauer, F.A. A silicon powder diffraction standard reference material. *J. Appl. Cryst.* **1975**, *8*, 45–48. [[CrossRef](#)]
50. Klug, H.P.; Alexander, L.E. *X-ray Diffraction Procedures for Polycrystalline and Amorphous Materials*, 5th ed.; John Wiley & Sons, Inc.: New York, NY, USA; London, UK; Sydney, NSW, Australia, 1967; pp. 491–538.
51. Williamson, G.K.; Hall, W.H. X-ray line broadening from filed aluminium and wolfram. *Acta Metall. Mater.* **1953**, *1*, 22–31. [[CrossRef](#)]
52. Madhu, G.; Bose, V.C.; Maniammal, K.; Aiswarya Raj, A.; Biju, V. Microstrain in nanostructured nickel oxide studied using isotropic and anisotropic models. *Physica. B* **2013**, *421*, 87–91. [[CrossRef](#)]
53. Kurllyandskaya, G.V.; Svalov, A.V.; Fernandez, E.; Garcia-Arribas, A.; Barandiaran, J.M. FeNi-based magnetic layered nanostructures: Magnetic properties and giant magnetoimpedance. *J. Appl. Phys.* **2010**, *107*, 09C502. [[CrossRef](#)]

54. Zhukov, A.; Talaat, A.; Ipatov, M.; Blanco, J.; Zhukova, V. Tailoring of magnetic properties and GMI effect of Co-rich amorphous microwires by heat treatment. *J. Alloys Comp.* **2014**, *615*, 610–615. [[CrossRef](#)]
55. Zhukov, A.; Ipatov, M.; Talaat, A.; Blanco, J.M.; Zhukova, V. Tailoring of Magnetic Properties and GMI Effect of Amorphous Microwires by Annealing. In *Sensing Technology: Current Status and Future Trends III*, 1st ed.; Mason, A., Chandra Mukhopadhyay, S., Padmarani Jayasundera, K., Eds.; Springer: Cham, Switzerland; Heidelberg, Germany; New York, NY, USA; Dordrecht, The Netherlands; London, UK, 2015; Volume 11, Smart Sensors, Measurement and Instrumentation; pp. 399–423, ISBN 978-3-319-10947-3.
56. Škorvánek, I.; Marcin, J.; Krenický, T.; Kováč, J.; Švec, P.; Janičkovič, D. Improved soft magnetic behaviour in field-annealed nanocrystalline Hitperm alloys. *J. Magn. Magn. Mater.* **2006**, *304*, 203–207. [[CrossRef](#)]
57. Škorvánek, I.; Marcin, J.; Turčanová, J.; Kováč, J.; Švec, P. Improvement of soft magnetic properties in Fe₃₈Co₃₈Mo₈B₁₅Cu amorphous and nanocrystalline alloys by heat treatment in external magnetic field. *J. Alloys Comp.* **2010**, *504S*, S135–S138. [[CrossRef](#)]
58. Škorvánek, I.; Marcin, J.; Capik, M.; Varga, M.; Turčanová, J.; Kováč, J.; Švec, P.; Janičkovič, D.; Kováč, F.; Stoyka, V. Tailoring of functional properties in Fe-based soft magnetic alloys by thermal processing under magnetic field. *Magneto hydrodynamics* **2012**, *48*, 371–377.
59. Blázquez, J.S.; Marcin, J.; Franco, V.; Conde, A.; Škorvánek, I. Influence of microstructure on the enhancement of soft magnetic character and the induced anisotropy of field annealed HITPERM-type alloys. *J. Appl. Phys.* **2015**, *117*, 17A301. [[CrossRef](#)]
60. Yang, Z.; Chlenova, A.A.; Golubeva, E.V.; Volchkov, S.O.; Guo, P.; Shcherbinin, S.V.; Kurlyandskaya, G.V. Magnetoimpedance Effect in the Ribbon-Based Patterned Soft Ferromagnetic Meander-Shaped Elements for Sensor Application. *Sensors* **2019**, *19*, 2468. [[CrossRef](#)]
61. Yoon, S.S.; Kim, C.G. Separation of reversible domain-wall motion and magnetization rotation components in susceptibility spectra of amorphous magnetic materials. *Appl. Phys. Lett.* **2001**, *78*, 3280–3282. [[CrossRef](#)]
62. Hernando, B.; Sánchez, M.L.; Prida, V.M.; Tejedor, M.; Vázquez, M. Magnetoimpedance effect in amorphous and nanocrystalline ribbons. *J. Appl. Phys.* **2001**, *90*, 4783–4790. [[CrossRef](#)]
63. Kuźmiński, M.; Lachowicz, H.K. Evolution of transverse permeability with DC-field in Co-based metallic glass ribbons. *J. Magn. Magn. Mater.* **2003**, *267*, 35–41. [[CrossRef](#)]
64. Laurita, N.; Chaturvedi, A.; Bauer, C.; Jayathilaka, P.; Leary, A.; Miller, C.; Phan, M.-H.; McHenry, M.E.; Srikanth, H. Enhanced giant magnetoimpedance effect and field sensitivity in Co-coated soft ferromagnetic amorphous ribbons. *J. Appl. Phys.* **2011**, *109*, 07C706. [[CrossRef](#)]
65. Sahoo, T.; Mishra, A.C.; Srinivas, V.; Nath, T.K.; Srinivas, M.; Majumdar, B. Enhanced magnetoimpedance and field sensitivity in microstructure controlled FeSiCuNbB ribbons. *J. Appl. Phys.* **2011**, *110*, 083918. [[CrossRef](#)]
66. Chaturvedi, A.; Laurita, N.; Leary, A.; Phan, M.-H.; McHenry, M.E.; Srikanth, H. Giant magnetoimpedance and field sensitivity in amorphous and nanocrystalline (Co_{1-x}Fe_x)₈₉Zr₇B₄ (x = 0, 0.025, 0.05, 0.1) ribbons. *J. Appl. Phys.* **2011**, *109*, 07B508. [[CrossRef](#)]
67. Dufay, B.; Saez, S.; Dolabdjian, C.; Yelon, A.; Men, D. Development of a High Sensitivity Giant Magneto-Impedance Magnetometer: Comparison with a Commercial Flux-Gate. *IEEE Trans. Magn.* **2013**, *49*, 85–88. [[CrossRef](#)]

Disclaimer/Publisher's Note: The statements, opinions and data contained in all publications are solely those of the individual author(s) and contributor(s) and not of MDPI and/or the editor(s). MDPI and/or the editor(s) disclaim responsibility for any injury to people or property resulting from any ideas, methods, instructions or products referred to in the content.